Journal of
Materials Chemistry A
Materials for energy and sustainability

This article can be cited before page numbers have been issued, to do this please use: S. Panugamti, B. Akkinepally, S. Prabu, C. S. Sale, G. Nagaraju and J. Shim, *J. Mater. Chem. A*, 2026, DOI: 10.1039/D6TA01506A.

ROYAL SOCIETY
OF CHEMISTRY

rsc.li/materials-a

View Article Online
DOI: 10.1039/D6TA01506A

Bioinspired value-added conversion of rotten bread into porous vanadium oxide-vanadium carbide@carbon composites for high-rate Zn- and Li-ion batteries

Sateesh Panugamti,[a] Bhargav Akkinepally,[a]* Samikannu Prabu,[b] Chandra Sekhar Sale,[d] Nagaraju Goli,[c]*Jaesool Shim[a]*

[a]*School of Mechanical Engineering, Yeungnam University, Gyeongsan 38541, Republic of Korea*

[b]*School of Chemical, Biological and Battery Engineering, Gachon University, 13120 Seongnam, Republic of Korea*

[c]*Department of Materials, Imperial College London, South Kensington Campus, London-SW7 2AZ, United Kingdom*

[d]*School of Chemical, Materials, and Biological Engineering, The University of Sheffield, Sheffield S1 3JD, United Kingdom*

Address corresponds to:

bhargav@ynu.ac.kr (B.A.);

nagarajugoli7@gmail.com (N.G);

jshim@ynu.ac.kr (J.Shim)

View Article Online
DOI: 10.1039/D6TA01506A

Abstract

The rapid accumulation of food waste has emerged as a pressing environmental challenge, motivating the development of sustainable strategies for waste valorization. Developing sustainable routes to transform discarded food-waste into functional electrode materials offers an effective solution to these challenges while supporting the growing demand for advanced battery technologies. In this work, we report a simple, scalable, and cost-effective approach to convert rotten bread into a highly porous vanadium oxide-vanadium carbide/carbon (VO-VC) composite through an infiltration and *in-situ* thermal process. Unlike conventional multistep routes that rely on post-synthetic carbon coating, our method enables the simultaneous formation of a conductive carbon framework and electroactive vanadium-based VO-VC heterostructures, which ensures intimate interfacial contact and enhanced electrochemical kinetics. In particular, the synergistic integration of VO and VC on porous carbon generates abundant heterointerfaces, enables lower charge transfer resistance and higher diffusion coefficients ($\sigma = 6.47\times10^{-13}$ cm^2 s^{-1}) during the Li-ion energy storage. As a result, the optimized VO-VC@800 electrode exhibits excellent electrochemical performance when evaluated as a Li-ion battery anode, delivering a high reversible capacity of 759.2 mAh g^{-1} at 0.1 A g^{-1} with a good rate capability of 407.8 mAh g^{-1} at 1 A g^{-1}, and long-term cycling stability (9.5% capacity loss) after 100 cycles and the electrode still showed good cycling stability after 450 cycles. Moreover, the same electrode demonstrates robust performance in aqueous zinc-ion batteries, achieving a high specific capacity of 170 mAh g^{-1} along with stable cycling and good rate characteristics, benefiting from rapid Zn^{2+} transport and structural integrity. Overall, our work demonstrates a viable waste-to-watts materials strategy and highlights the potential of biomass-derived metal oxide-carbon composites for sustainable rechargeable battery applications.

Keywords: Food waste; vanadium oxide-vanadium carbide; pseudocapacitive charges; lithium-ion batteries; zinc-ion batteries

View Article Online
DOI: 10.1039/D6TA01506A

1. Introduction

Recently, Li-ion batteries (LiBs) have attracted global demand as efficient and high-performing energy storage systems for portable electronics, electric vehicles, and grid-storage markets. [1–3] Conventionally, LiBs based cells were assembled using graphite-based layered anodes, which have limitations in terms of theoretical performance.[4,5] Especially, graphite delivers a relatively low theoretical specific capacity of 372 mAh g^{-1},[6,7] which restricts further improvements in energy density required for next-generation high-power and long-range applications.[8] Additionally, lithium dendrite formation, sluggish lithium-ion dynamics at high current densities, and limited rate capability under fast charging conditions continue to challenge graphite-based anode materials. These limitations have motivated intensive research into alternative anode materials that can offer higher capacity, faster ion transport, and improved cycling stability.[9–11] In parallel, there is growing interest in the development of sustainable zinc-ion batteries (ZiBs) for portable electronic sensors because of their high safety, natural abundance, and low cost of materials, along with its high theoretical capacity and aqueous electrolyte compatibility.[12–14] However, similar to LiBs, the development of high-performance electrode materials remains a critical challenge for ZiBs, particularly in achieving long cycling life and stable electrochemical kinetics.[15] Recently, transition metal oxides, owing to their multiple oxidation states, rich redox chemistry, and high theoretical capacities, have emerged as promising candidates for both Li- and Zn-ion energy storage systems.[16,17]

Among various metal oxides, vanadium-based materials have attracted significant attention due to their wide redox range ($V^{5+} \leftrightarrow V^{4+} \leftrightarrow V^{3+}$), flexible crystal structures, and strong redox activity, which collectively enable high charge storage capability.[18–20] Vanadium oxides, such as VO_2, V_2O_5, and V_6O_{13}, have demonstrated excellent electrochemical properties arising from their layered/tunnel-type frameworks, which facilitate metal-ion intercalation and diffusion.[21–23] However, these materials are often hindered by intrinsic drawbacks such as low

View Article Online
DOI: 10.1039/D6TA01506A

electronic conductivity, structural instability during repeated cycling, and severe volume expansion/contraction during metal-ion insertion and extraction.[24] To address these issues, various strategies have been explored, including heteroatom doping, composite formation with conductive carbon and graphene. Among these approaches, constructing carbon-metal oxide composites has proven particularly effective, as conductive carbon matrices can buffer volume changes, enhance electrical conductivity, and improve structural integrity during long-term cycling.[25–27] However, most of the research focused on metal oxides that are initially synthesized and subsequently combined with carbon or graphene through post-treatment processes, which often involve multiple steps, higher energy consumption, and increased cost.[28,29] In contrast, the *in-situ* formation of carbon-metal oxide composites through a single-step and or integrated synthesis route offers a more efficient and scalable approach. Such strategies enable intimate interfacial contact between the carbon framework and active metal oxide phases, leading to improved charge transport kinetics and structural stability with long-term cycling stability. Therefore, developing facile, low-cost, and sustainable synthesis routes for battery materials is highly desirable for next-generation energy storage systems.

On the other hand, food waste has been considered a significant fraction of global municipal waste, which represents an abundant and renewable carbon resource that remains largely underutilized for energy storage devices.[30] Converting food waste into advanced electrode materials not only addresses environmental and waste-management concerns but also provides a low-cost and sustainable route for energy material synthesis. Among the various food waste sources, bread waste is generated in enormous quantities worldwide and is rich in carbonaceous compounds, making it an attractive precursor for porous carbon frameworks.[31] When subjected to controlled metal precursor immersion and thermal treatment, bread-derived biomass can yield carbon@metal oxide conductive composites with high surface area, hierarchical porosity, and abundant defect sites, all of which are beneficial for electrochemical energy storage. Integrating such biomass-derived carbon@metal oxide compounds offers a promising pathway toward high-performance and sustainable battery electrodes. For example, Zhan et al., synthesized MnO@C composite as anode material for LiBs using rice husk as biowaste, which delivered excellent capacity of 1104 mAh g^{-1} with a capacity retention of 830 mAh g^{-1} after 200 cycles.[32] In another work, Li et al., used surgical medical masks derived carbon with NiO nanocomposite for Li-ion batteries, which delivered a maximum capacity of 420 mA h g^{-1} after 800 cycles at a current density of 0.2 A g^{-1}.[33] Furthermore, Dai et al., used coconut meat derived carbon with molybdenum sulfide composite as high-performance anode for LiBs, which showed a good cycling capacity of 720.1 mAh g^{-1} after 200 cycles.[34] Considering the advantage of carbon-metal oxide composites, it is also important to develop vanadium-based compounds combined with carbon matrices derived from food waste, which present a unique opportunity to synergistically enhance the electrochemical performance of batteries. The presence of carbon improves electrical conductivity and structural stability, while vanadium oxides/carbides provide high redox activity and reversible ion storage capability.

In this work, we report a sustainable and scalable strategy for synthesizing vanadium oxide-vanadium carbide on carbon (VO-VC) composite materials using rotten bread as both a carbon source and structural template. Through a simple impregnation of bread with vanadium precursor followed by controlled carbonization at elevated temperatures, highly porous VO-VC@carbon composites with interconnected conductive networks were obtained. The resulting materials exhibit a unique architecture in which VO_2 nanoparticles are uniformly embedded within a carbon matrix derived from waste bread, while partial carbothermal reduction leads to the formation of vanadium carbide (V_6C_5). The heterostructured VO-VC composite on porous carbon effectively combines the advantages of high redox activity, enhanced electrical conductivity, and robust structural stability. The electrochemical performance of the as-prepared materials was systematically investigated in both LiBs and

ZiBs, demonstrating improved capacity, rate capability, and cycling stability compared to pristine vanadium oxide counterparts. Overall, our work showed a viable approach for converting food waste into high-value energy storage materials, and it provides cost-effective methodologies for the design of other metal oxide-carbon composite-based multifunctional electrodes for next-generation rechargeable batteries

2. Results and discussion

Value-added conversion of food waste into energy materials is highly desirable owing to the enormous global generation of food waste, its inefficient disposal pathways, and the associated environmental and economic burdens, while simultaneously offering a sustainable route to transform abundant, renewable biowaste into high-performance functional electrode materials for next-generation battery applications. Figure 1 shows the schematic and photographic images of the food waste (rotten bread) derived vanadium oxide-vanadium carbide (VO-VC) composite material using a simple soaking and pyrolysis process. As we know, bread is a widely discarded food waste generated in large quantities worldwide in homes/restaurants, and they often disposed of in household bins, landfills or low-value waste streams (pie chart in Figure 1a).[35] Such disposal not only leads to food resource loss but also contributes to environmental burdens, including greenhouse gas emissions. Figure 1a shows the photographic image of the rotten bread (RB), which is a widely generated food waste, emphasizing its global abundance and underutilization. The porous, sponge-like microstructure of bread, formed through yeast fermentation during baking, provides an intrinsically interconnected three-dimensional framework that is highly suitable for hosting metal precursor species. For the conversion of RB into energy storage materials, initially, the ethanol-washed RB pieces of rotten bread are immersed in an aqueous vanadyl sulfate ($VOSO_4$) solution (Figure 1b). During the soaking process, $VOSO_4$ solution was infiltrated into the internal pore channels of the bread matrix through capillary action and diffusion. The abundant hydroxyl-containing functional

View Article Online
DOI: 10.1039/D6TA01506A

groups present in starch and protein components of bread facilitate coordination and adsorption of vanadium species, ensuring uniform precursor distribution throughout the scaffold. After soaking for 1 h, the solvent is removed via evaporation (at 75 °C), leading to the decoration of $VOSO_4$ within and on the surface of the bread framework (Figure 1c). The dried RB-$VOSO_4$ material is subsequently mechanically blended into a fine powder to improve homogeneity and ensure consistent thermal treatment. The blending process eliminates macroscopic bread morphology while retaining the microscopic porous characteristics inherited from the bread structure. Afterwards, the RB-$VOSO_4$ powder was thermally treated in a tube furnace under an inert argon atmosphere, as shown in Figure 1d. The inert environment prevents excessive oxidation of carbon and enables controlled carbothermal reactions. During annealing at elevated temperatures, the organic components of the bread undergo pyrolysis to generate porous carbon, while the vanadium precursor undergoes simultaneous reduction with carbon and phase transformation to form vanadium oxide-vanadium carbide (VO-VC)@carbon composites. For comparison, vanadium oxide (VO) was also synthesized in the absence of rotten bread, as present in Figure 1e. Without the carbon scaffold, the resulting bulk VO exhibits dense, stacked morphology with limited porosity, which further shows the critical role of bread-derived VO-VC material in regulating microstructure and preventing particle agglomeration. Without $VOSO_4$, the annealed bread led to the formation of porous carbon, which exhibits porous morphology, as presented in the SEM images of Figure S4. For Comparison a control sample derived from a conventional carbon precursor(glucose)was synthesized and included in the revised supporting information file Figure S8. Figures 1f and 1g illustrate the VO-VC composite materials obtained at carbonization temperatures of 700 °C and 800 °C (denoted as VO-VC@700 and VO-VC@800), respectively. At high temperatures under inert atmosphere, the RB-$VOSO_4$ with carbothermal reduction leads to the partial conversion of vanadium oxide (VO) into vanadium carbide (VC), while a fraction of vanadium oxide is retained in the carbon matrix, forming a heterostructured composite (VO-VC@carbon). The VC domains are uniformly dispersed within the conductive porous carbon matrix, while residual vanadium oxide contributes redox-active sites. The as-synthesized VO-VC exhibits a rough, interconnected network with abundant meso- and macropores (Figure 1g), which originate from the bread native cellular structure and gas evolution during pyrolysis. Such a morphology is advantageous for electrochemical applications, as it provides high surface area, short diffusion pathways for ions, and effective accommodation of volume changes during cycling. Figure 1h displays the photographic images of the powder samples obtained from different synthesis routes, including bare vanadium oxide, VO-VC@700, and VO-VC@800. The darker appearance of VO-VC@carbon composites indicates higher carbonization and enhanced electrical conductivity relative to bare vanadium oxide. Collectively, Figure 1 demonstrates a simple, scalable, and sustainable strategy for converting rotten bread into high-performance VO-VC@carbon composite electrode materials.

The crystallinity and phase structures of the samples were analyzed using X-ray diffraction (XRD). Figure 2a shows the XRD diffraction peaks of the bare VO (synthesized without rotten bread) sample, which were well indexed to V_6O_{13} (JCPDS No: 01-075-1140), confirming the formation of a monoclinic crystalline structure. The sharp and intense peaks located at 2θ degrees of 26.8°, 25.3°, 45.6°, 17.8°, 15.1°, 30.1°, and 33.4°, corresponding to the characteristic crystal peaks of (0 0 3), (1 1 0), (-6 0 1), (0 0 2), (2 0 0), (-4 0 1), and (3 1 0) planes of V_6O_{13}, respectively, indicating high crystallinity and well-ordered structure.[36] Its XRD crystal structure presented in Figure 2b also demonstrates that the mixed-valence V^{4+}/V^{5+} framework corresponds to V_6O_{13}, as it possesses layered arrangements of distorted VO_6 octahedra, favourable for reversible ion insertion. Upon carbonization (at 700 and 800 °C) of the $VOSO_4$-impregnated bread precursor, the samples showed mixed phases of vanadium oxide (VO_2) and vanadium carbide (V_6C_5) peaks with broad carbon diffraction peaks (Figure 2c).

View Article Online
DOI: 10.1039/D6TA01506A

The sample synthesized at 700 °C shows strong intensities for VO_2 peaks but very low intensities for VC peaks, which indicates that the growth temperature is not high enough to crystallize the material. When the temperature is increased to 800 °C, the diffraction peak with the 2θ degrees of 37.4°, 43.5° and 63.2° were related to hexagonal crystalline structure of V_6C_5 (JCPDS NO: 01-080-2287)[37] and XRD peaks observed at 31.6°, 44.4°, and 55.3° were corresponding to the VO_2 with characteristic crystallographic planes of (1 3 0), (1 0 1) (2 1 0), and (2 1 1) conforming to the formation of tetragonal structure of VO_2 (JCPDS NO: 01-071-0291).[38] Additionally, the broad peaks with crystallographic planes of (0 0 2) and (0 0 4) were observed at 26.4 ° and 43.0 ° confirms the existence of carbon in the prepared VO-VC@carbon composite. From the XRD spectra in Figure 2c, it is evident that the VO-VC@700 and VO-VC@800 samples showed diminished peaks related to V_6O_{13}, while new diffraction peaks corresponding to VO_2 and V_6C_5 phases emerge. The new phase transformation in the bread-derived material suggests partial reduction and carburization of the vanadium oxide framework during high-temperature annealing, facilitated by the carbonaceous species generated from bread pyrolysis. The structural evolution is further clarified through crystal structure models, where VO_2 adopts a distorted rutile-type framework with edge- and corner-sharing VO_6 octahedra (Figure 2d), offering open channels favourable for Li^+ diffusion. The V_6C_5 phase (Figure 2e), on the other hand, possesses a dense carbide lattice that enhances electrical conductivity and structural robustness. The coexistence of VO_2 and V_6C_5 within a carbonaceous scaffold could be beneficial to provide a synergistic heterostructure that balances redox activity and electronic transport, which is crucial for high-performance electrochemical behaviour. The Raman spectra of the bare VO and the VO-VC@carbon composite were recorded to investigate the structural characteristics and bonding environment (Figure 2f). The bare VO sample exhibited several characteristic vibrational bands corresponding to V-O stretching and bending vibrations at 81.7, 402.9, 675.3, 860.4, 987.9, and 1093.6 cm^{-1}. Upon

View Article Online
DOI: 10.1039/D6TA01506A

carbonization at 700 and 800 °C, new Raman bands emerge, including the prominent D and G bands of carbon located near 1358.2 cm^{-1} and 1587.1 cm^{-1}, which correspond to the disordered carbon (sp^3- hybridized) and graphitic carbon (sp^2-hybridized) structures. The increased intensity ratio of the D to G band (I_D/I_G) at higher carbonization temperature indicates a higher degree of structural disorder and the formation of defect-rich carbon domains. Meanwhile, the attenuation of V-O vibrational modes reflects partial reduction of vanadium oxides and the formation of mixed-valence VO_2 species embedded within the carbon matrix. Nitrogen (N_2) adsorption-desorption measurements reveal distinct textural differences between bare VO and the VO-VC@carbon (800 °C) composite (Figures 2g-i). The pristine VO exhibits a relatively low specific surface area (<5 m^2 g^{-1}) with a type-II isotherm, which is characteristic of non-porous or weakly porous solids with unrestricted multilayer adsorption and negligible capillary condensation (Figure 2g). In contrast, the VO-VC@800 sample shows a high surface area of 391.1 m^2 g^{-1} with a type-IV isotherm accompanied by a pronounced hysteresis loop, indicating the presence of a well-developed mesoporous structure where capillary condensation occurs within confined pores (Figure 2h). The corresponding pore size distribution confirms abundant mesopores in the few-nanometer range, originating from the decomposition of the bread-derived carbon matrix and the release of gaseous species during thermal treatment (Figure 2i). These interconnected mesopores significantly enhance electrolyte penetration, improve ion diffusion kinetics, and shorten diffusion pathways, thereby contributing to the superior electrochemical performance of the VO-VC@800 composite.

The surface morphology and elemental analysis of bare VO and RB-derived VO-VC samples were analysed using scanning electron microscopy (SEM), as presented in Figure 3. Figure 3a-c shows the SEM images of bare VO synthesized in the absence of rotten bread. At low magnification (Figure 3a), the synthesized VO exhibits irregularly shaped, micron-sized agglomerates composed of densely stacked brick-like structures with a lateral size of ~5-10

View Article Online
DOI: 10.1039/D6TA01506A

μm. The higher-magnification SEM images in Figures 3b and 3c further reveal smooth, flat surfaces with minimal surface roughness and a lack of discernible porosity at the nanoscale. Such dense morphologies are typically associated with restricted electrolyte penetration and sluggish ion diffusion, which are unfavourable for electrochemical energy storage applications. In contrast, SEM images of VO-VC@700, synthesized by carbonization of the RB-$VOSO_4$ precursor at 700 °C shows different surface morphology (Figures 3d-f) compared to the bare VO. At low magnification (Figure 3d), the composite exhibits a highly textured and irregular morphology characterized by interconnected frameworks and rough surfaces. Unlike bare VO, the presence of bread-derived VO-VC@carbon showed the porous morphology with nanoparticle formation on the porous architecture. The increased magnifications (Figure 3e and 3f) reveal numerous nanoscale vanadium oxide and vanadium carbide particles uniformly distributed and anchored onto the carbon matrix. Figures 3g-i present SEM images of VO-VC@800, obtained by increasing the carbonization temperature to 800 °C. The overall morphology shown in Figure 3g retains the interconnected porous framework observed in VO–VC@700 but with more pronounced structural definition and increased surface roughness. The higher magnification image in Figure 3h exhibits a well-developed porous carbon skeleton, within which vanadium-based nanoparticles are more uniformly and densely distributed. Compared to VO-VC@700, the nanoparticles in VO-VC@800 appear more crystalline and slightly larger, suggesting enhanced carbothermal reduction and improved phase crystallinity at the higher temperature, as confirmed by the XRD analysis in Figure 2. Under the higher magnification, the VO-VC@800 (Figure 3i) further reveals the dense decoration of VO-VC nanoparticles throughout the porous carbon matrix, forming a continuous and conductive network. The hierarchical porosity, comprising micro- and mesopores, originates from both the intrinsic cellular structure of the bread and the release of gaseous species during carbonization. The intimate contact between the active vanadium species and the conductive porous carbon matrix is expected to enhance charge transfer kinetics and structural stability during electrochemical cycling. Figure 3j shows the elemental analysis of VO-VC@800 using energy-dispersive X-ray spectroscopy (EDX). The EDX spectrum (Figure 3j(i)) confirms the presence of vanadium (V), oxygen (O), and carbon (C) as the major constituent elements, verifying the successful formation of VO-VC composites embedded in a carbon matrix. In addition, trace amounts of sodium (Na) and sulfur (S) are detected, which could be attributed to residual salts naturally present in bread, while S originates from the sulfate group of the $VOSO_4$ precursor. The corresponding elemental mapping images (Figures 3j(ii-vi)) reveal a uniform spatial distribution of the constituent elements. Carbon mapping image in Figure 3j(ii) confirms a continuous carbon framework derived from rotten bread, while vanadium is homogeneously dispersed (Figure 3j(iii)), indicating well-anchored VO-VC nanoparticles within the carbon matrix. Oxygen mapping overlaps with vanadium, confirming the coexistence of vanadium oxide and carbide phases (Figure 3j(iv)). Sodium and sulfur exhibit low intensity yet uniform signals, consistent with their trace presence originating from bread residues and the $VOSO_4$ precursor.

The TEM analysis was carried out to further understand the crystallinity and microstructure of the prepared sample. The TEM images presented in Figure 4a-b clearly demonstrate that the VO-VC particles were successfully decorated onto a porous carbon matrix as the carbon support exhibits a highly porous, interconnected structure. As shown in the bright-field TEM image (Figure 4b), the VO-VC particles appear randomly distributed over the carbon framework, indicating effective dispersion and strong interaction with the carbon support. Such porous conductive architecture of VO-VC@800 could be expected to provide a large surface area and facilitates mass and charge transport during the electrochemical process. The high-resolution TEM images (Figure 4c-d) further reveal structural details where the VO-VC regions show clear and well-defined lattice fringes, confirming their crystalline nature,

View Article Online
DOI: 10.1039/D6TA01506A

whereas the surrounding carbon displays a diffuse contrast without distinct lattice fringes, characteristic of an amorphous structure. These observations confirm the formation of crystalline VO-VC nanoparticles embedded within an amorphous porous carbon matrix. The thermal evolution and phase transformation behavior of the $VOSO_4$-rotten bread precursor during the carbonization process was evaluated using the thermogravimetric-differential thermal analysis (TGA-DTA). Figure 4e shows the TGA profile of the precursor, which shows an initial weight loss below 200 °C, which is attributed to the removal of physically adsorbed moisture and loosely bound water molecules originating from the dissolved water, hydrated $VOSO_4$ salt, and the porous bread matrix. The second weight loss occurring between ~250-350 °C arises from the decomposition of organic components originating from the bread matrix and partial decomposition of $VOSO_4$ species. The third and major weight loss, observed between 400-700 °C, happens from the carbonization of the food waste bread and the concurrent reduction of vanadium species. In this temperature range, carbon derived from the bread acts as a reducing agent, converting vanadium oxides partially into lower-valence phases and enabling the *in-situ* formation of vanadium carbide (V_6C_5). Beyond 700 °C, the mass stabilizes, indicating completion of carbonization and carbide formation, consistent with the development of a stable VO-VC@carbon composite structure. Figure 4f shows the X-ray photoelectron spectroscopy (XPS) survey spectrum of VO-VC@carbon, which further confirms the elemental composition of the final composite, revealing the presence of V, O, and C as the dominant elements, with no detectable impurity phases. The strong C 1s signal reflects the carbon-rich framework derived from the bread precursor, while the pronounced V 2p and O 1s peaks confirm the successful incorporation of vanadium oxide species. Figure 4g shows the high-resolution XPS spectra of the V 2p region and O 1s regions. In particular, the deconvoluted V $2p_{3/2}$ and V $2p_{1/2}$ peaks reveal characteristic binding energies (516.97 and 524.30 eV) corresponding to mixed-valence vanadium species, primarily V^{4+} with a minor

View Article Online
DOI: 10.1039/D6TA01506A

contribution from V^{5+}. The dominance of V^{4+} is consistent with the formation of VO_2 as the primary phase after thermal treatment, while the minor V^{5+} component may arise from surface oxidation or residual oxygen-rich environments.[39,40] In the same spectra, the O 1s spectrum further supports this interpretation, exhibiting multiple components corresponding to lattice oxygen (V-O-V), surface oxygen species, and oxygen-containing functional groups associated with the carbon matrix. The main O 1s peak at lower binding energy (531.27 eV) is attributed to lattice oxygen in VO_2, while higher binding energy contributions arise from surface hydroxyls or C-O functionalities.[41] The surface oxygen species can improve interfacial wettability with the electrolyte and promote ion transport. The high-resolution C 1s spectrum in Figure 4h displays distinct components associated with sp^2-hybridized carbon (C=C), sp^3-hybridized carbon (C-C), and oxygen-containing functional groups such as C-O and C=O. The dominance of the sp^2 carbon peak indicates the formation of a conductive graphitic-like carbon framework during carbonization, which is essential for enhancing electronic conductivity and structural integrity. The presence of oxygenated carbon species suggests partial surface functionalization, which can facilitate stronger interaction between the carbon matrix and VO_2 nanoparticles.

Using the rotten-bread-derived VO-VC@carbon composite and bare VO electrodes, the Li-ion storage performance was evaluated and compared (Figure 5). Coin-type LIB cells were assembled using VO-VC@carbon composites and bare VO as working electrodes, lithium metal as the counter/reference electrode, and $LiPF_6$ dissolved in ethylene carbonate/diethyl carbonate as the electrolyte. Figure 5a presents the galvanostatic charge-discharge profiles of the VO-VC@carbon (VO-VC@800) electrode measured at various current densities ranging from 0.1 to 2.0 A g^{-1} within a voltage window of 0.01-3.0 V (vs. Li^+/Li). During the first discharge cycle at 0.1 A g^{-1}, the electrode delivers a high specific capacity, which is accompanied by noticeable irreversible capacity loss in the subsequent cycle. The initial

View Article Online
DOI: 10.1039/D6TA01506A

capacity decay is primarily attributed to the formation of a solid electrolyte interphase (SEI) layer and irreversible Li consumption associated with surface reactions between the electrolyte and the porous VO-VC@carbon matrix.[42] From the 2nd cycle onward, the charge-discharge curves exhibit good overlap and stable voltage plateaus, indicating the formation of a stable SEI and highly reversible Li- insertion/extraction processes. As the current density increases (0.1-2.0 A g^{-1}), the discharge capacity gradually decreases (759.2 mAh g^{-1} to 301.2 mAh g^{-1}), which is a typical kinetic limitation arising from reduced lithium-ion diffusion time at higher rates. Nevertheless, even at 2.0 A g^{-1}, VO-VC@800 retains a substantial capacity of (301.2 mAh g^{-1}), reflecting excellent rate tolerance. The charge-discharge curves of bare VO and VO-VC@700-based cells at different current densities are included in Figure S1. The CV and charge-discharge curves of bread-derived carbon (bare carbon) at varied scan rates and current densities are presented in Figure S5. The differential capacity (*dQ/dV*) plots shown in Figure 5b further provide the redox behaviour of bare VO, bare carbon, VO-VC@carbon (VO-VC@700), and VO-VC@800 electrodes during the battery testing. Specifically, bare VO exhibits low intensity weak redox peaks, indicative of sluggish reaction kinetics and poor reversibility. In contrast, both VO-VC@carbon composites display more pronounced and well-defined redox peaks, particularly VO-VC@800, which shows sharper peaks and reduced polarization. These features correspond to multistep Li-ion intercalation/deintercalation reactions associated with vanadium redox couples in the VO-VC@carbon composite. The enhanced peak intensity and reduced peak separation in VO-VC@800 suggest faster charge-transfer kinetics and improved electrochemical reversibility, enabled by the conductive carbon matrix and the presence of vanadium carbide, which enhances electronic conductivity. Figure 5c compares the 2nd cycle charge-discharge profiles of bare VO, bare carbon, VO-VC@700, and VO-VC@800 electrodes at a current density of 0.1 A g^{-1}. Bare VO delivers a relatively low reversible capacity with steep voltage slopes, reflecting limited active sites and poor Li-

View Article Online
DOI: 10.1039/D6TA01506A

ion accessibility.[43] In contrast, bare carbon shows improved capacity due to its better electrical conductivity and porous structure, which promotes efficient ion transport and electron movement. However, the composites based on VO-VC and carbon samples exhibit higher capacity compared to the bare VO and carbon. Specifically, the VO-VC@800 demonstrates the highest discharge capacity over VO-VC@700 and other solitary samples. The enhanced performance of VO-VC@800 can be attributed to its optimized composite structure, where densely decorated vanadium oxide nanoparticles provide rich redox-active sites, vanadium carbide improves electronic conductivity, and the porous carbon framework facilitates rapid Li-ion transport. The comparative discharge capacities from the 1st to 2nd cycles were summarized in Figure 5d. Specifically, bare VO shows a low initial capacity and substantial irreversible capacity loss, highlighting its structural instability and poor interfacial compatibility with the electrolyte. In contrast, bare carbon performs better than bare VO due to its improved conductivity and porous nature. However, the VO-VC@700 exhibits higher capacity than the bare VO and bare carbon, while VO-VC@800 delivers the highest first-cycle capacity and significantly improved capacity retention into the 2nd cycle than the remaining comparative samples. This trend emphasizes the importance of food waste carbonization along with vanadium composites in tailoring the porous conductive architecture and electrochemical energy storage performance. Rate capability measurements are presented in Figure 5e, where the electrodes are subjected to stepwise current densities from 0.1 to 1.0 A g^{-1} and subsequently returned to 0.1 A g^{-1}. Bare VO shows rapid capacity decay even at low current densities, confirming its poor rate performance (100 mAh g^{-1} at 0.1 A g^{-1}; 4.5 mAh g^{-1} at 1.0 A g^{-1}). Simultaneously, the bare carbon exhibits much better rate capability (653.01 mAh g^{-1} at 0.1 A g^{-1}; 14.7 mAh g^{-1} at 1.0 A g^{-1}). Compare to these solitary electrodes, the composites based on VO-VC@700 displays moderate rate capability (722.4 (1st cycle)/347.8 mAh g^{-1} (2nd cycle) at 0.1 A g^{-1}; 47.4 mAh g^{-1} at 1.0 A g^{-1}), whereas VO-VC@800 exhibits superior performance

View Article Online
DOI: 10.1039/D6TA01506A

(733.2 mAh g^{-1} (1st cycle)/766.1 mAh g^{-1} (2nd cycle) at 0.1 A g^{-1}; 407.8 mAh g^{-1} at 1.0 A g^{-1}), maintaining high capacities across all tested rates and demonstrating excellent capacity recovery (745.4 mAh g^{-1}) when the current density is reverted to 0.1 A g^{-1}. The outstanding rate behaviour (55.6%) reflects the robust electrode architecture, where the interconnected porous VO-VC and carbon network ensures continuous electron pathways and short lithium-ion diffusion lengths. The effect of carbon precursor (commercial glucose-derived anodes) on electrochemical performance in comparison with our bread-derived sample also showed significant deviation in terms of capacity and interfacial charge storage resistance (details were given in Figure S8). Electrochemical impedance spectroscopy (EIS) results shown in Figure 5f further support the enhanced charge transport properties of the VO-VC@carbon composite compared to the bare VO- and bare carbon-based LIB cells. The Nyquist plots consist of a semicircle in the high-to-medium frequency region, corresponding to charge-transfer resistance (R_{ct}), followed by a sloped line at low frequencies associated with Li-ion diffusion. Bare VO exhibits the largest semicircle diameter, indicating high R_{ct} (260.4Ω), and the bare carbon showed a smaller semicircle compared to bare VO with the R_{ct} of 202.2Ω. In contrast, VO-VC@700 and VO-VC@800 show significantly reduced R_{ct} values (198.4 and 186.2Ω), with VO-VC@800 displaying the smallest semicircle, confirming the most efficient interfacial charge-transfer kinetics. The ion diffusion kinetics were investigated from the linear relationship between $Z'$and $\omega^{-1/2}$ in the low-frequency region (Figures S9a-b) from which the Warburg coefficient (σ) was caluculated using the following equation. [44]

$$D = \frac{R^2T^2}{2A^2n^4F^4C^2\sigma^2} \tag{6}$$

Where R is the gas constant, T is the absolute temperature, A is the electrode area, n is the number of electrons transferred in the redox couple, F is the Faraday's constant, C is the ion Concentration of $Li^{+,}\sigma$ is the Warburg coefficient. Among all electrodes, VO-VC@800

View Article Online
DOI: 10.1039/D6TA01506A

exhibited the lowest Warburg coefficient (σ =116.337), indicating faster Li^+ transport and improved electrochemical kinetics due to the optimized conductive carbon network and enhanced electrolyte accessibility. Accordingly, the Li^+ diffusion coefficient of VO-VC@800 is 6.47×10^{-13} cm^2 s^{-1} was higher than that of bare VO and VO-VC@700 (4.65×10^{-13} cm^2 s^{-1}) confirming the beneficial role of the VO/carbon heterostructure in facilitating ion diffusion and charge transfer. After cycling, the VO-VC@800 electrode showed a significant reduction in the σ from 116.337 to 10.157 (Figure S9b), accompanied by a remarkable increase in the Li^+ diffusion coefficient to 8.49×10^{-11} cm^2 s^{-1}. This improvement suggests electrochemical activation and interfacial reconstruction during cycling, which create more accessible transport pathways and additional electroactive sites[45]. We believe that improved conductivity and diffusion coefficients in the VO-VC@800 is attributed to the conductive vanadium carbide phase and the continuous carbon matrix derived from food waste RB. In addition, the interfacial electronic structure between VO and VC within the conductive carbon matrix plays an important role in enhancing charge transfer kinetics and pseudocapacitive behaviour. The formation of VO-VC heterointerfaces induces charge redistribution and built-in electric fields, which facilitate rapid electron transport across the interface. The metallic nature of VC improves electrical conductivity, while VO provides abundant redox-active sites for Li-ion storage. The corresponding synergistic interaction between VO and VC within the carbon matrix lowers charge-transfer resistance and promotes surface-controlled redox reactions and improves rate capability during fast cycling. The EIS plots of the corresponding samples after cycling stability were also shown in Figure S2. Figure 5g shows the long-term cycling stability of the fabricated cells at a current density of 0.1 A g^{-1} for 100 cycles. As shown in Figure 5g, bare VO exhibits low capacity with poor cycling stability. Meanwhile, VO-VC@700 shows improved capacity compared to bare VO but still noticeable capacity decay from 1st to 2nd cycle, with stable capacity after prolonged cycling. Remarkably, VO-VC@800 exhibits a high reversible capacity with only 9.5% capacity loss and a coulombic efficiency of ~98% during the initial 100 cycles. However, during extended cycling up to 450 cycles (Figure S3), the electrode exhibits a more significant capacity fading of approximately 50.5%, suggesting a gradual decline in electrochemical stability upon prolonged charge-discharge cycling. The post-cycling XRD patterns confirm the stable crystal structure of the VO-VC electrode after prolonged cycling (Figure S3d). The retained characteristic peaks indicate good structural integrity during repeated ion insertion/extraction, while slight peak broadening suggests mild surface reconstruction and enhanced electroactive behavior. Moreover, the absence of impurity phases or severe structural collapse demonstrates the excellent stability of the VO-VC heterostructure. The excellent cycling stability is attributed to the structural robustness of the VO-VC@800 electrode, where the porous carbon matrix buffers volume changes during repeated lithiation/delithiation, while strong interfacial bonding between VO-VC nanoparticles and carbon prevents particle pulverization and detachment from the current collector. Figure 5h schematically illustrates the internal structure of the LIB assembly and structural advantages of the VO-VC@800 electrode during the electrochemical process. Firstly, the three-dimensional porous carbon framework derived from rotten bread provides abundant ion-accessible channels and continuous electron-conducting pathways. Secondly, the uniformly distributed VO-VC nanoparticles on carbon act as active sites for Li-ion storage. Lastly, VC enhances electronic conductivity and structural integrity to enable the capacity retention at high rates and cycling stability. The synergistic architecture of VO-VC@carbon facilitates rapid Li-ion diffusion, efficient charge transfer, and stable electrochemical reactions, collectively accounting for the superior Li-ion storage performance observed for VO-VC@800.

The electrochemical evaluation of the Li-storage behavior of the VO-VC@800 electrode in comparison with previously reported vanadium-based anode materials were presented in Figure 6a and Table S1. As presented in Figure 6a, the initial and long-term

View Article Online
DOI: 10.1039/D6TA01506A

reversible capacities of various vanadium-based anodes in comparison with VO-VC@800 show our composite material demonstrated good capacity and cycling stability, which can be attributed to the synergistic interaction between the conductive carbon matrix and the electroactive vanadium oxide phases. The inset in Figure 6a shows the photograph image of VO-VC@800-based LiB. Utilizing the high capacity and high voltage of 3.0 V, the battery successfully powers a red color light-emitting diode, confirming its ability to deliver stable energy output under real working conditions. Figure 6b shows cyclic voltammetry (CV) curves of the V_6O_{13} (bare VO) electrode recorded at different scan rates (0.1-1.0 mV s^{-1}), revealing a low-current response with multiple redox peaks associated with reversible multistep lithium-ion insertion and extraction processes. At a scan rate of 0.1 mV s^{-1}, VO exhibited the oxidation peaks at 0.25, 1.2, and 2.4V, and while the reduction peaks were identified at the peak voltages of 1.75, 1.0, and 0.48 V, respectively, which correspond to sequential phase transitions and redox reactions of vanadium-ions with variable oxidation states ($V^{5+}/V^{4+}/V^{3+}$), which are characteristic of vanadium-based electrodes.[46] The gradual increase in peak current with scan rate indicates good electrochemical reversibility and fast charge-transfer kinetics. The relationship between peak current (i) and scan rate (v) follows the power-law relationship (Figure 6c). According to the power law, $i = av^b$, where a and b are adjustable constants; the value of b indicates the dominant charge storage mechanism: if $b = 0.5$ corresponds to diffusion-controlled behaviour, while $b = 1.0$ suggests surface-controlled (capacitive) processes.[47] The calculated b-values of the bare VO show the mixed charge storage process, signifying a dominant pseudocapacitive and diffusion-limited contribution. Figure 6d shows the CV curves of the VO-VC@800 electrode at different scan rates (0.1-1.0 mV s^{-1}), which exhibit similar redox features but with significantly enhanced current responses compared to bare VO. For the VO-VC@800, both materials can store Li^+ through intercalation/deintercalation during cycling. The cathodic peaks are attributed to the lithiation

View Article Online
DOI: 10.1039/D6TA01506A

of VO_2 and V_6C_5 to Li_xVO_2 and (eq. 1 and 2), while the anodic peaks were obtained due to the delithiation process (oxidation; eq. 3 and 4) in the reverse reactions, as shown below. [48]

$$VO_2 + xLi^+ + xe^- \rightarrow Li_xVO_2 \quad (1)$$

$$V_6C_5 + yLi^+ + ye^- \rightarrow Li_yV_6C_5 \quad (2)$$

$$Li_xVO_2 \rightarrow VO_2 + xLi^+ + xe^- \quad (3)$$

$$Li_yV_6C_5 \rightarrow V_6C_5 + yLi^+ + ye^- \quad (4)$$

From the CV curves under increased current densities, the current density was also increased with reduced polarization, which indicates faster electron transport and improved ionic accessibility in the VO-VC@carbon composite. The corresponding b-values shown in Figure 6e further confirm the mixed charge-storage mechanism, with a substantial capacitive contribution arising from surface-controlled processes and a diffusion-limited contribution arising from the VO material in the composite. To further quantify the capacitive and diffusion-controlled contributions from the VO-VC@800, the total current response was separated using the modified power equation:[49]

$$i(V) = k_1\nu + k_2\nu^{1/2} \quad (5)$$

Where $k_1\nu$ represents the capacitive-controlled current and $k_2\nu^{1/2}$ corresponds to diffusion-limited processes (Figure S6). As shown in Figure 6f, the VO-VC@800 electrode exhibits a dominant capacitive contribution across the tested scan rates, confirming that the porous carbon framework and nanosized VO-VC facilitate rapid surface redox reactions and efficient ion transport. The calculated capacitive- and diffusion-limited contribution of VO-VC@800-based LiB was plotted in Figure 6e. Evidently, the evolution of capacitive contribution with increasing scan rate reveals a progressively higher pseudocapacitive fraction at higher sweep rates (from 66.6% to 83.7%). The enhanced electrochemical performance of VO-VC@800 can therefore be attributed to its hierarchical porous structure, high electrical conductivity, and strong interfacial coupling between VO-VC nanoparticles and the carbon matrix.

Furthermore, VO-VC@800 has been explored as a potential electrode material for Zn-ion batteries (ZiBs), as vanadium-based materials were extensively used as cathode materials.[50] **Figure 7**a schematically depicts the assembled Zn//VO-VC@800-based ZiB, where the porous VO-VC@800 cathode was paired with a metallic Zn anode and a 3M aqueous $Zn(CF_3SO_3)_2$ electrolyte with a piece of glassy fiber paper as a separator. Figure 7b shows the CV curves of the VO-VC@800-based cell recorded at various scan rates ranging from 0.1 to 1.0 mV s^{-1}, which display well-defined and highly reversible redox peaks, indicating a stable Zn^{2+} insertion/extraction process. The presence of multiple redox peaks corresponds to stepwise redox transitions associated with vanadium valence changes ($V^{5+}/V^{4+}/V^{3+}$) during Zn^{2+} intercalation and deintercalation.[51] Notably, the overall shape of the CV curves remains highly preserved even at increased scan rates from 0.1-1 mV s^{-1}, demonstrating fast reaction kinetics and excellent electrochemical reversibility. The gradual increase in peak current with scan rate further indicates the coexistence of surface-controlled capacitive behavior and diffusion-controlled intercalation processes. To quantitatively analyze the charge storage mechanism, the relationship between peak current (i) and scan rate (ν) was evaluated using the power-law equation. As shown in Figure 7c, the extracted b-values for both oxidation (0.87 and 0.91) and reduction (0.81 and 0.9) suggest that the charge storage process is dominated by capacitive behavior with a substantial contribution from diffusion-controlled intercalation. The hybrid charge storage mechanism arises from the synergistic effect of the nanostructured VO-VC domains and the conductive carbon matrix, which together provide abundant electrochemically active sites and shorten ion diffusion pathways. Figure 7d presents the galvanostatic charge-discharge profiles of the VO-VC@800 electrode at various current densities ranging from 0.1 to 1 A g^{-1}. The non-linear charge-discharge capacity plots with minimal voltage hysteresis

View Article Online
DOI: 10.1039/D6TA01506A

indicate highly reversible Zn^{2+} insertion/extraction kinetics and low polarization. At a current density of 0.1 A g^{-1}, the ZiB exhibits a maximum specific capacity of 170 mAh g^{-1} with a capacity retention of 149.7 mAh g^{-1} when the current density was increased to ten folds higher. Even at high current densities, the electrode maintains considerable capacity, revealing the robustness of the VO-VC@800 electrode architecture. The rate capability of the VO-VC@800 electrode is presented in Figure 7e, which demonstrates excellent capacity retention as the current density increases stepwise. Notably, when the current density is returned to its initial low value, the specific capacity recovers to its original level (174 mAh g^{-1}), evidencing outstanding structural stability and electrochemical reversibility. The EIS plots shown in Figure 7f further elucidate the favorable charge-transfer characteristics of the VO-VC@800 electrode. Specifically, the Nyquist plots of the VO-VC@800 electrode after the cycling process exhibit significantly reduced charge transfer resistance compared to the fresh cell, which could be attributed to the electrochemical activation and high conductivity of the composite electrode in the fabricated ZiBs. In-situ electrochemical impedance spectroscopy (EIS) was performed at different states of the charge-discharge process to understand the charge storage kinetics of the material, as shown in Figure 7f. Specifically, the in-situ EIS plots of the ZIB reflect the voltage-dependent reaction mechanism governing charge storage kinetics of the VO-VC@800 composite. Starting from OCV, the relatively large semicircle indicates higher charge-transfer resistance (R_{ct}) due to limited electroactive sites utilization. Upon charging to higher potentials (up to 1.6 V), progressive oxidation of vanadium species (V^{3+}/V^{4+} to higher valence states) activates additional redox sites at the VO-VC heterointerface. This is accompanied by a continuous decrease in R_{ct}, suggesting facilitated electron transfer enabled by the conductive VC phase and improved interfacial charge redistribution. Concurrently, the Warburg region becomes steeper, indicating faster ion diffusion as electrolyte ions access the porous carbon network and heterostructured interfaces. Meanwhile, during the discharge process (1.6 V to 0.2

View Article Online
DOI: 10.1039/D6TA01506A

V), the reduction reactions were dominated at the VO-VC electrode, involving Zn-ion insertion into the oxide lattice and partial occupation of active sites, which leads to a moderate increase in R_{ct}, reflecting slower kinetics associated with diffusion-controlled processes. On the contrary, at lower discharge voltage (0.8-0.2 V), the R_{ct} further decreases instead of increasing. This behavior suggests that the electrode undergoes a kinetically favorable reduction process, where ion insertion leads to increased electrical conductivity and improved electrode/electrolyte contact. The reduced vanadium states and the metallic contribution from the carbide phase facilitate faster electron transport, while the porous carbon framework ensures efficient ion accessibility. This indicates that the charge storage at these potentials is predominantly governed by surface-controlled pseudocapacitive reactions rather than sluggish solid-state diffusion. However, the absence of a significant impedance rise indicates that the porous carbon framework effectively accommodates volume changes and maintains electrical connectivity. Overall, the potential-dependent impedance evolution demonstrates a coupled mechanism where fast surface redox reactions at VO-VC heterointerfaces dominate, supported by diffusion-assisted ion insertion, with the carbon matrix ensuring continuous electron transport and structural stability. For the Zn-ion battery system (Figure S9c), the Zn^{2+} diffusion coefficient slightly decreased from 10^{-15} to 10^{-14} cm^2 s^{-1} at different applied voltages, which were included in Table S3. The difference in diffusion coefficients could be attributed to the larger ionic size and stronger electrostatic interaction of Zn^{2+} ions during repeated insertion/extraction. Nevertheless, the stable diffusion behavior demonstrates the structural robustness of the VO-VC@800 electrode. The equivalent circuit model (Figure S9d), including solution resistance (R_1), charge-transfer resistance (R_2), constant phase element (Q_2), Warburg diffusion element (W_2), and capacitive component (C_3), further confirms the improved charge-transfer kinetics and ion diffusion capability of the optimized VO-VC@800 electrode. The long-term cycling performance of the Zn//VO-VC@800 cell was presented in Figure 7g.

Noticeably, the device showed highly stable capacity retention (82.7%) over prolonged cycling, with minimal capacity decay and coulombic efficiency of 97.1%. The higher cycling stability of VO-VC@800-based ZiBs further demonstrates the structural integrity of the composite electrode, which could effectively mitigate vanadium dissolution, electrode pulverization, and electrode-electrolyte interface degradation during repeated Zn^{2+} storage processes. Finally, the practical feasibility of the VO-VC@800 electrode is demonstrated by assembling two Zn//VO-VC@800 cells in series to power a red color LED, as shown in Figure 7h. The higher energy storage performance and cycling stability of waste-derived VO-VC@carbon-based composites for both Li-ion and Zn-ion energy storage systems provide a viable way for advanced and cost-effective electrode materials for practical applications.

3. Conclusion

In summary, a sustainable and scalable strategy has been developed to convert waste bread into a high-performance VO-VC@carbon composite electrode through a simple infiltration of vanadium precursors and a subsequent carbonization process. When used as an electrode material for rechargeable batteries, the porous VO-VC@carbon composite with the interconnected carbon framework derived from food waste provides a robust conductive network, while the uniformly distributed heterostructured VO-VC phases synergistically enhance redox activity, ion diffusion, and electrical conductivity. As a result, the VO-VC@800 electrode exhibits excellent electrochemical performance in Li-ion batteries, delivering a high reversible capacity of 759.2 mAh g^{-1} at 0.1 A g^{-1}, excellent rate capability of 407.8 mAh g^{-1} at 1 A g^{-1}, and remarkable cycling stability with good coulombic efficiency over prolonged cycling. For zinc-ion batteries, the VO-VC@800 was further examined, which demonstrates high-rate capability with a reversible capacity of 170 mAh g^{-1} at 0.1 A g^{-1}, and good cycling durability, retaining stable structural features over extended cycles. The mixed charge storage contribution, reduced charge-transfer resistance, and stable electrode-electrolyte interface

View Article Online
DOI: 10.1039/D6TA01506A

collectively account for the superior performance in both battery systems. Overall, our work provides the feasibility of transforming food waste into high-value electrode materials and opens a new avenue for developing next-generation rechargeable batteries with a reduced environmental footprint.

4. Experimental Section

4.1. Materials

Vanadium oxide sulphate hydrate ($VOSO_4.H_2O$), N-methyl-2-pyrrolidinone, $LiPF_6$ (lithium hexafluorophosphate) dissolved in a mixture of EC (ethylene carbonate) and DMC (dimethyl carbonate (MTI Korea), Zinc trifluoromethanesulfonate ($(CF_3SO_3)_2Zn$; Sigma Aldrich), polyvinylidene difluoride (PVdF), Super P carbon black (MTI Korea) and Li/Zn foils (MTI Korea) were received and used without any further purification. Expired bread was collected from the local restaurants in Yeungnam University, Gyeongsan area.

4.2. Synthesis of waste rotten-bread-derived vanadium oxide-vanadium carbide@carbon (VO-VC@carbon) composite: Waste rotten bread-derived value-added vanadium oxide-vanadium carbide on porous carbon (VO-VC@carbon) was synthesised using a simple impregnation and pyrolysis process. Initially, expired rotten bread (RB) pieces were collected (10 g) and washed with ethanol a few times and dried in an oven at 70 °C for 4 h. Simultaneously, $VOSO_4$ (2.2 g) was dissolved in 70 mL of deionized water under continuous magnetic stirring for 30 min at room temperature. The dried, rotten bread was subsequently immersed in the $VOSO_4$ solution to ensure uniform adsorption of the vanadium species. The impregnated sample was subjected to solvent evaporation at 75 °C for 12 h, resulting in a dried composite precursor. The precursor was then thermally treated at 700-800 °C for 2 h in a tubular furnace under a constant argon flow (100 ccm min^{-1}) with a heating rate of 5 °C min^{-1}. During the high-temperature treatment, the bread was converted into carbon, and the $VOSO_4$ was converted into vanadium oxide. Additionally, the biomass-derived carbon simultaneously acted as a reducing agent, which facilitated the carbothermal conversion of vanadium oxide into vanadium carbide. The resulting final compound, VO-VC@carbon was collected after naturally cooling the furnace to room temperature. The products were thoroughly washed with deionized water and ethanol to remove residual impurities and subsequently dried at 80 °C for 6h. For comparison, the vanadium oxide (V_6O_{13}; VO) without using rotten bread pieces and bare carbon without using vanadium precursor (Figure S4) were also synthesized under the same temperature conditions. The effect of carbon precursor on morphology and electrochemical features was also compared with commercial glucose sample (details were given in Figure S9).

4.3. Characterization

The structure and morphology of bare VO and VO-VC@carbon precursors were characterized by X-ray diffraction (XRD, PANlytical; 40 kV and 30 mA) and scanning electron microscopy (SEM, Hitachi S4800) equipped with energy-dispersive X-ray spectroscopy (EDX). SEM images were recorded at a voltage of 10kV. The chemical composition and oxidation states of elements were evaluated using the X-ray photoelectron spectroscopy (XPS; Thermofisher). High-resolution transmission electron microscope (HR-TEM, Tecnai G^2; 300 kV.) was used to identify the microstructure and crystallinity of the prepared samples. The surface area and textural properties were evaluated by nitrogen adsorption and desorption isotherms (BET analyser; Micromeritics (3-FLEX) with Barrett-Joyner-Halenda (BJH) method. The electronic state and vibrational fingerprints of the prepared VO-VC@carbon and bare VO were identified Raman spectroscopy analyser (Horiba (XploRA). Thermogravimetric analysis-differential thermal analysis (TGA-DTA; Ta Instruments (SDT Q600) is used to study the $VOSO_4$-bread precursor physical and chemical changes with temperature.

4.4. Electrochemical measurements: The Electrochemical performance was evaluated using CR2032-type coin cells assembled in the glove box. The working electrodes were prepared by mixing the active material (VO-VC@carbon or bare VO), conductive carbon (Super P), and polyvinylidene difluoride (PVdF) binder in a typical ratio 8:1:1 using N-methyl-2 pyrrolidone (NMP) as the solvent. The homogeneous slurry was cast onto the copper foil and titanium foil current collectors and dried under vacuum at 75° C for 12h. The mass loading of the active material was 2 mg on the current collector. Lithium and zinc foils were employed as counter/reference electrodes, separated by separators. The electrolytes consisted of $LiPF_6$ (lithium hexafluorophosphate) dissolved in a mixture of EC (ethylene carbonate) and DMC (dimethyl carbonate) for Li-ion battery; 3M Zinc trifluoromethanesulfonate ($Zn(CF_3SO_3)_2$)-based electrolyte for Zn-ion batteries were used. Galvanostatic charge-discharge (GCD) tests were performed within the voltage range 0.01-3V (LIBs) and 0.2-1.6 V (zinc-ion battery) under different current densities. Cyclic Voltammetry (CV) at different scan rates and electrochemical impedance spectroscopy (EIS) were conducted over a range of 100 kHz to 0.1 Hz on the fabricated battery cells. All electrochemical measurements were conducted at room temperature (approximately 25 °C) using Biologic and a Wonatech electrochemical workstation with the assembled battery cells.

Acknowledgments

This work was supported by the National Research Foundation (NRF) of Korea, which is funded by the Korean Government (No. RS-2023-00280665). The first author, S.P., would like to thank Dr Mohan Reddy Pallavolu (Gachon University) for his thoughtful suggestions on the characterization of this work.

References:

1 A. Manthiram, *ACS Cent. Sci.*, 2017, **3**, 1063–1069.

2 M. Broussely and G. Archdale, *J. Power Sources*, 2004, **136**, 386–394.

View Article Online
DOI: 10.1039/D6TA01506A

3 C. P. Grey and D. S. Hall, *Nat. Commun.*, 2020, **11**, 6279.

4 Y. Dong, C. Liu, M. Rui, X. Zhang, Y. Guan, L. Chen, Q. Huang, M. Wang, Y. Su, F. Wu and N. Li, *Adv. Funct. Mater.*, DOI:10.1002/adfm.202506190.

5 Y. Dong, F. Wu, T. Chen, Y. Su, S. Weng, C. Liu, W. Yan, S. Ma, L. Chen, Q. Huang, B. Wang, Y. Guan, X. Wang and N. Li, *Adv. Energy Mater.*, DOI:10.1002/aenm.202500978.

6 J. Xie and Y.-C. Lu, *Nat. Commun.*, 2020, **11**, 2499.

7 J. Asenbauer, T. Eisenmann, M. Kuenzel, A. Kazzazi, Z. Chen and D. Bresser, *Sustain. Energy Fuels*, 2020, **4**, 5387–5416.

8 G. Nagaraju, P. Santhoshkumar, S. C. Sekhar, B. Ramulu, M. Nanthagopal, P. S. S. Babu, C. W. Lee and J. S. Yu, *J. Power Sources*, 2022, **549**, 232113.

9 E. R. Buabeng and D. A. Noye, *ECS Meeting Abstracts*, 2022, **MA2022-02**, 2604–2604.

10 K. Yuan, Y. Lin, X. Li, Y. Ding, P. Yu, J. Peng, J. Wang, H. Liu and S. Dou, *ENERGY & ENVIRONMENTAL MATERIALS*, DOI:10.1002/eem2.12759.

11 G. A. Collins, H. Geaney and K. M. Ryan, *J. Mater. Chem. A Mater.*, 2021, **9**, 14172–14213.

12 B. Zhang, X. Cai, J. Li, H. Zhang, D. Li, H. Ge, S. Liang, B. Lu, J. Zhao and J. Zhou, *Energy Environ. Sci.*, 2024, **17**, 3878–3887.

13 S. Javed, G. Suo, L. Habib, C. Lin, J. Li, X. Hou, X. Ye, Y. Yang and S. Ding, *J. Energy Storage*, 2025, **118**, 116271.

14 C. Chen, K. Lu, Y. Wang, R. Cheng, T. Xiang, M. Xia, F. Wang, W. Lei, J. Yang, S. Mathur and Q. Hao, *ACS Appl. Mater. Interfaces*, 2025, **17**, 23860–23871.

15 L. E. Blanc, D. Kundu and L. F. Nazar, *Joule*, 2020, **4**, 771–799.

16 Y. M. Plotnikov and Dm. M. Korotin, *Journal of Physics and Chemistry of Solids*, 2026, **208**, 113172.

17 R. Hidayat, S. Aftab, A. Khalid, H. H. Hegazy, A. H. Rajpar, N. Rubab and M. A. Yewale, *J. Alloys Compd.*, 2025, **1039**, 183257.

18 Y. Kim, Y. Park, M. Kim, J. Lee, K. J. Kim and J. W. Choi, *Nat. Commun.*, 2022, **13**, 2371.

19 P. Hu, P. Hu, T. D. Vu, M. Li, S. Wang, Y. Ke, X. Zeng, L. Mai and Y. Long, *Chem. Rev.*, 2023, **123**, 4353–4415.

20 B. Wan, Y. Wang, X. Chen, C. Zhan, H. Jiang, J.-H. Liu, Y. Gao, X. Jiang, X. Cao, H. Zhang, S.-X. Dou and Y. Xiao, *Chem. Sci.*, 2025, **16**, 8217–8239.

View Article Online
DOI: 10.1039/D6TA01506A

21 J. Cao, T. Ou, S. Geng, X. Zhang, D. Zhang, L. Zhang, D. Luo, X. Zhang, J. Qin and X. Yang, *J. Colloid Interface Sci.*, 2024, **656**, 495–503.

22 H. Maclennan, B. Marckx and Ö. Ö. Capraz, *MRS Commun.*, 2025, **15**, 1040–1045.

23 Y. Zhang, B. Zhao, Z. Li, Z. Guo and M. Liu, *Mater. Today Chem.*, 2024, **36**, 101946.

24 S. Li, B. Lv, J. Gao, X. He and J. Wang, *J. Alloys Compd.*, 2025, **1021**, 179721.

25 T. Song, W. Fan, Y. Hu, H. Zhang and Y. Bai, *Green Chemistry*, 2025, **27**, 10071–10093.

26 H. Zhou, J. Wang, L. Shen, P. Liang, X. Xu, B. Li, Z. Zhang, X. Zhu, Z. Kong, J. Guo, D. Ji, L. Yu, K. Yan, L. Hu and K. Zhu, *Advanced Materials*, DOI:10.1002/adma.202514323.

27 Z. Gan, X. Ren, M. Liu, N. Wang, T. Pian, M. Sun, C. Jia and Z. Li, *Chemical Engineering Journal*, 2025, **506**, 160013.

28 P. Pazhamalai, V. Krishnan, M. S. Mohamed Saleem, S.-J. Kim and H.-W. Seo, *Nano Converg.*, 2024, **11**, 30.

29 P. Guo, L. Singer, Z. Zhao, W. Kukułka, F. Sebastian, E. Mijowska, M. Zharnikov, P. Comba and R. Klingeler, *Electrochim. Acta*, 2023, **459**, 142540.

30 J. M. Davidraj, C. I. Sathish, M. R. Benzigar, Z. Li, X. Zhang, R. Bahadur, K. Ramadass, G. Singh, J. Yi, P. Kumar and A. Vinu, *Sci. Technol. Adv. Mater.*, DOI:10.1080/14686996.2024.2357062.

31 J. M. Davidraj, C. I. Sathish, M. R. Benzigar, Z. Li, X. Zhang, R. Bahadur, K. Ramadass, G. Singh, J. Yi, P. Kumar and A. Vinu, *Sci. Technol. Adv. Mater.*, DOI:10.1080/14686996.2024.2357062.

32 D. Zhan, W. Luo, H.-B. Kraatz, M. Fehse, Y. Li, Z. Xiao, D. F. Brougham, A. J. Simpson and B. Wu, *ACS Omega*, 2019, **4**, 18908–18917.

33 G. Li, M. Ma, X. Chen, J. Zhang, Y. Hong, Y. Huan and T. Wei, *Energy & Fuels*, 2023, **37**, 702–710.

34 R. Dai, Y. Xu, P. Chen, X. Wang, T. Zheng, Y. Wang, D. Ruan and Z. Qiao, *Int. J. Electrochem. Sci.*, 2024, **19**, 100480.

35 J. Ananda, D. Pearson and S. Oakden, *J. Clean. Prod.*, 2024, **471**, 143377.

36 S. Wang, W. Wei, T. Huang, T. Zhang, Z. Chen, X. Chen and N. Dai, *Adv. Eng. Mater.*, DOI:10.1002/adem.201801374.

37 S. Lai, M. Gan, L. Xu, Z. Tan, Z. Li, S. Wei, Y. Jiang, J. Feng and X. Chong, *Surfaces and Interfaces*, 2023, **36**, 102573.

38 T. Han, Y. Wang, K. Tao, X. Zeng, P. Zhan, Y. Zhu, J. Li and J. Liu, *Chemical Communications*, 2024, **60**, 3918–3921.

39 I. P. Pinnock, Y. Fan, Y. Zhu, B. Narayan, T. Wang, I. P. Parkin and B. Deka Boruah, *J. Mater. Chem. A Mater.*, 2025, **13**, 1372–1383.

40 Y. Padwal, R. Chauhan, I. J. Chaudhary, D. J. Late, M. Ashokkumar and S. Gosavi, *Energy Advances*, 2025, **4**, 281–295.

41 H. Idriss, *Surf. Sci.*, 2021, **712**, 121894.

42 S. Zhang, N. S. Andreas, R. Li, N. Zhang, C. Sun, D. Lu, T. Gao, L. Chen and X. Fan, *Energy Storage Mater.*, 2022, **48**, 44–73.

43 H. Liu, P. He, J. Cao, T. Duan, Q. Kong and W. Yao, *J. Power Sources*, 2022, **521**, 230946.

44 E. Park, S. So and J. Hur, *Appl. Surf. Sci.*, 2022, **579**, 152182.

45 R. Córdoba, O. Dolotko, A. Kuhn and F. García-Alvarado, *J. Alloys Compd.*, 2024, **1002**, 175512.

46 S. Awasthi, S. Moharana, V. Kumar, N. Wang, E. Chmanehpour, A. D. Sharma, S. K. Tiwari, V. Kumar and Y. K. Mishra, *Nano Materials Science*, 2024, **6**, 504–535.

47 G. Nagaraju, S. C. Sekhar, B. Ramulu and J. S. Yu, *Energy Storage Mater.*, 2021, **35**, 750–760.

48 S. Castro-Pardo, A. B. Puthirath, S. Fan, S. Saju, G. Yang, J. Nanda, R. Vajtai, M. Tang and P. M. Ajayan, DOI:10.1039/d3ta06286d.

49 G. Nagaraju, S. C. Sekhar, B. Ramulu, Sk. K. Hussain, D. Narsimulu and J. S. Yu, *Nanomicro Lett.*, 2021, **13**, 17.

50 Y. Kim, Y. Park, M. Kim, J. Lee, K. J. Kim and J. W. Choi, *Nat. Commun.*, 2022, **13**, 2371.

51 T. Zhou, L. Xie, Q. Han, X. Qiu, Y. Xiao, X. Yang, X. Liu, S. Yang, L. Zhu and X. Cao, *Coord. Chem. Rev.*, 2024, **498**, 215461.

View Article Online
DOI: 10.1039/D6TA01506A

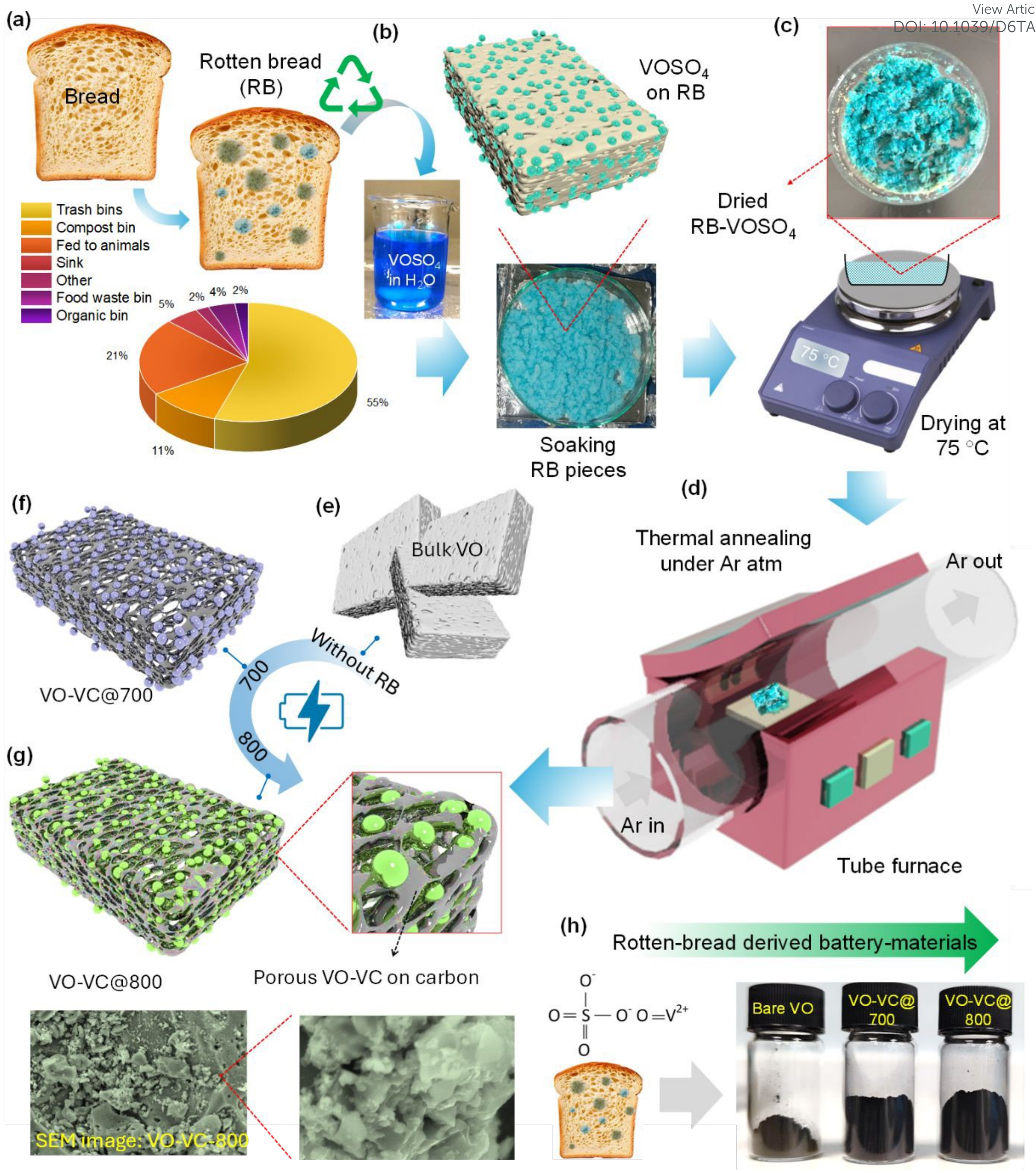

Figure 1. Schematic illustration of the sustainable synthesis of rotten-bread-derived vanadium oxide-vanadium carbide@carbon (VO-VC@carbon) composite-based battery materials. (a) photographic image of rotten bread and wastage percentage in homes/restaurants. (b) Immersion of rotten bread (RB) pieces in aqueous $VOSO_4$ solution enables infiltration and adsorption of vanadium precursor. (c) Formation of dried RB-$VOSO_4$ powder after solvent evaporation. (d) Thermal annealing of the RB-$VOSO_4$ powder in a tube furnace under an argon atmosphere. (e) Bulk vanadium oxide (V_6O_{13}; VO) was synthesized without bread as a control sample at 800 °C. (f,g) Formation of porous VO_2-V_6C_5 on carbon (VO-VC@carbon)

View Article Online
DOI: 10.1039/D6TA01506A

composites obtained at carbonization temperatures of 700 °C (VO-VC@700) and 800 °C (VO-VC@800), respectively. (h) Photographs of the resulting powder samples, including bare VO, VO-VC@700, and VO-VC@800.

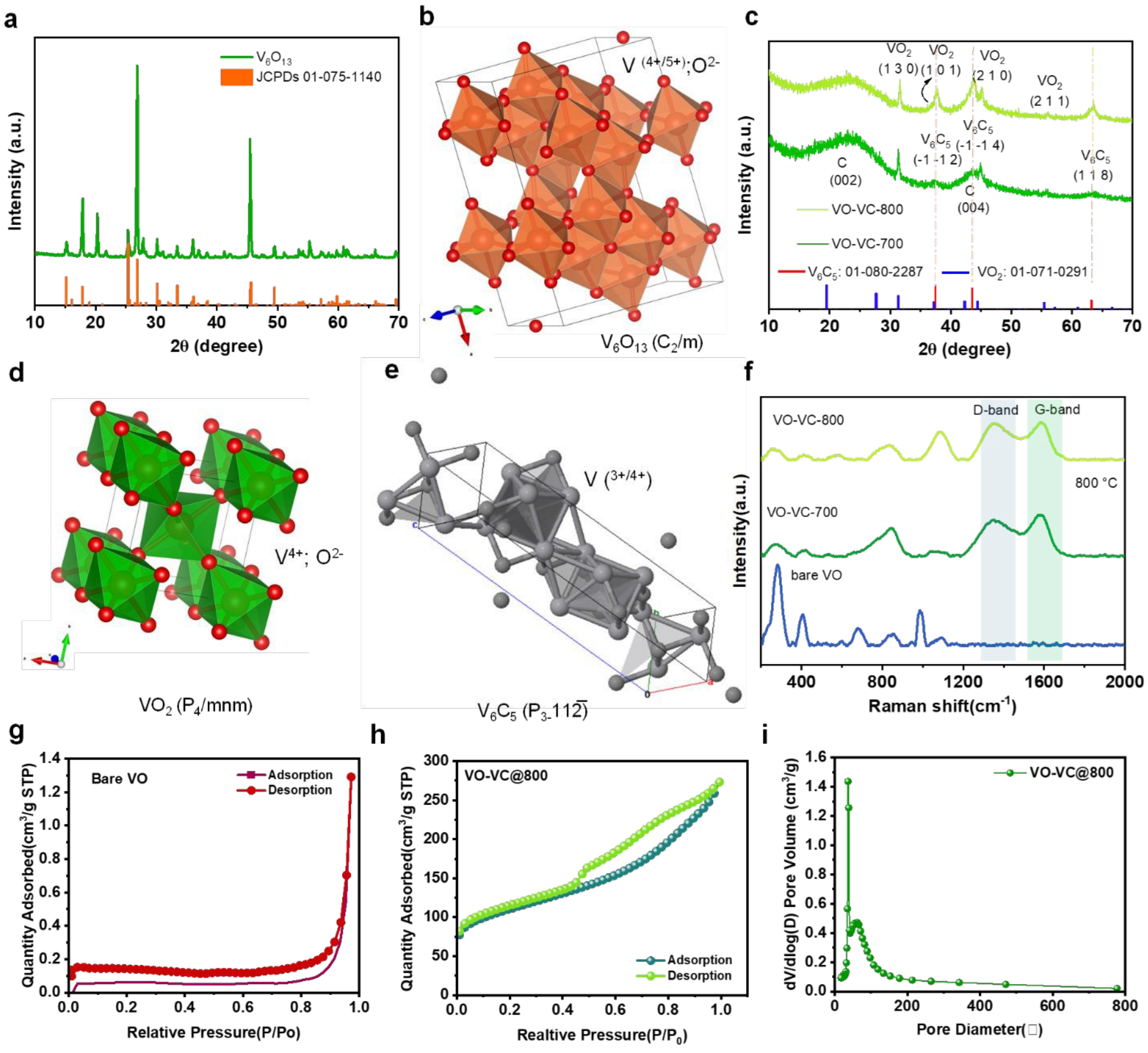

Figure 2. (a-e) X-ray diffraction (XRD) patterns of bare V_6O_{13} (VO), VO_2-V_6C_5 on carbon obtained at different temperatures of 700 and 800 °C (VO-VC@700, and VO-VC@800 samples) along with their crystal structures. f) Raman spectra of bare VO, VO-VC@700, and VO-VC@800. *(g-h) N_2 adsorption-desorption isotherms of bare VO and VO-VC@800. i) Corresponding pore size distribution of VO-VC@800.*

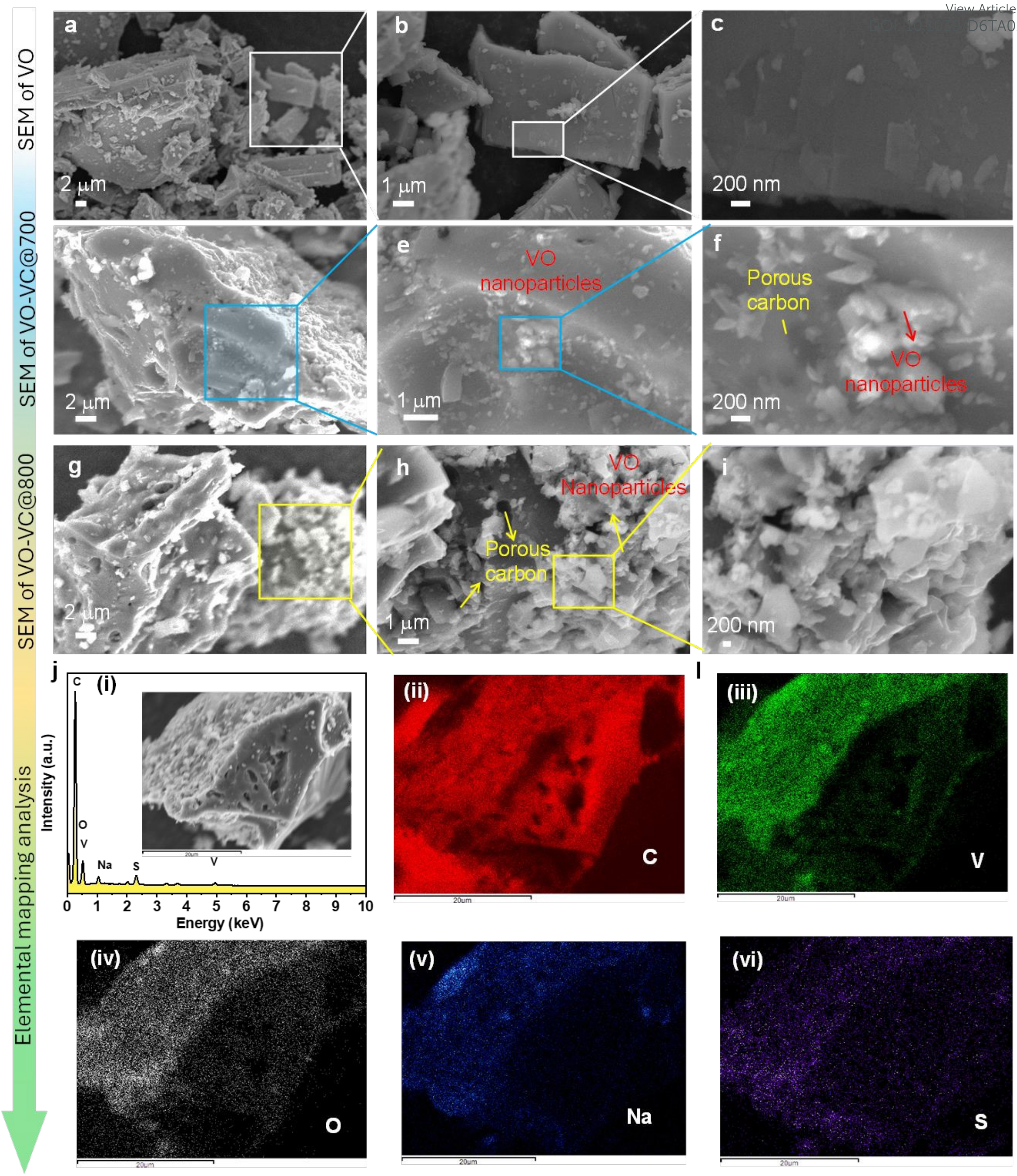

Figure 3. Morphological and compositional characterization of bare VO and rotten-bread-derived VO-VC@carbon composites. (a-c) SEM images of bare vanadium oxide (VO) synthesized without bread, showing dense and brick-like morphology. (d-f) SEM images of VO-VC@700 revealing porous carbon frameworks decorated with uniformly distributed VO-VC nanoparticles. (g-i) SEM images of VO-VC@800 showing enhanced porosity and dense decoration of VO-VC nanoparticles on the carbon matrix. (j)-(i) EDX spectrum confirming the presence of V, O, and C with trace Na and S, and (ii-vi) corresponding elemental mapping

View Article Online
DOI: 10.1039/D6TA01506A

images of C, V, O, Na, and S, demonstrating homogeneous elemental distribution throughout the composite.

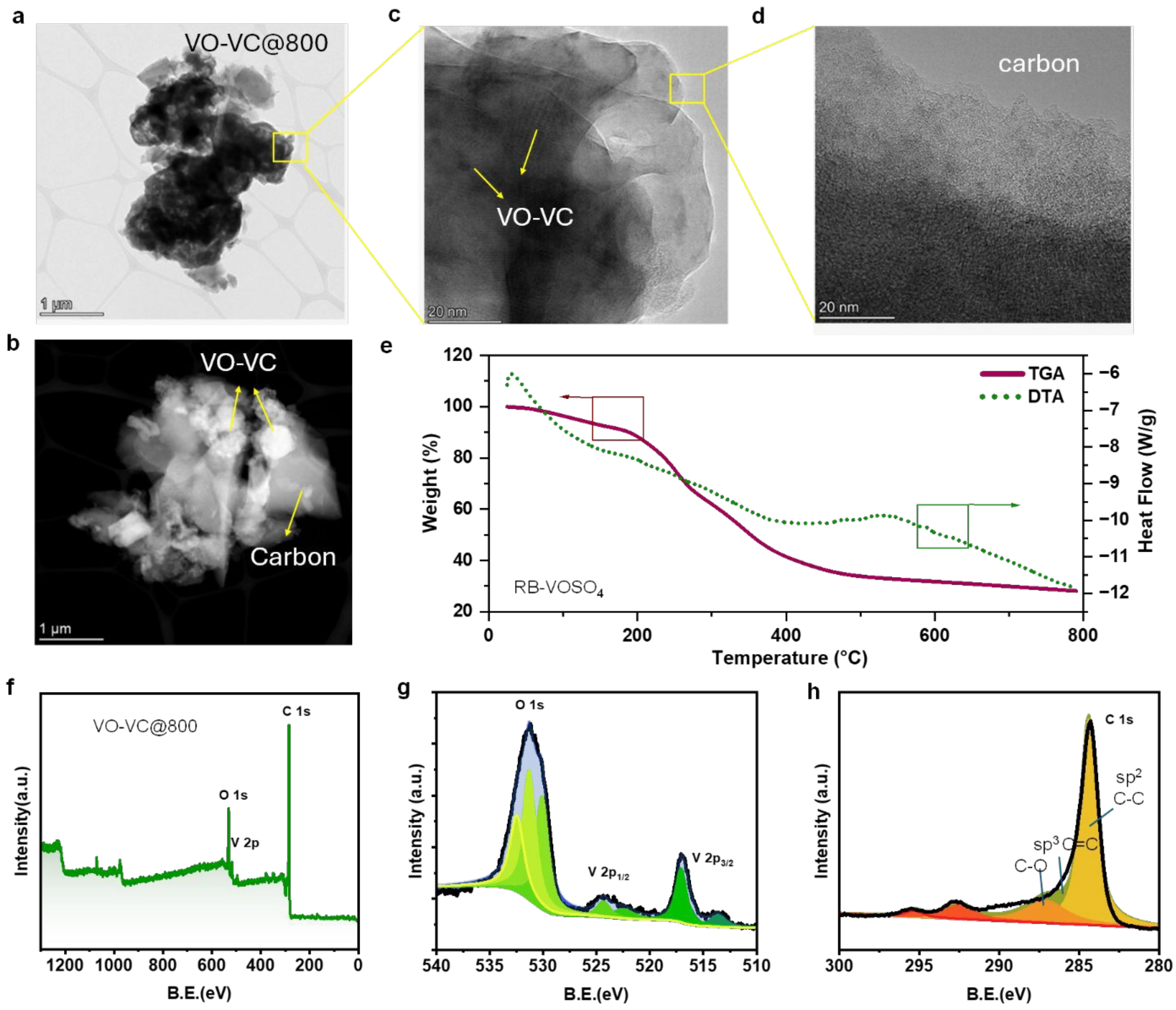

Figure 4. TEM, thermal and surface chemical analysis of RB-$VOSO_4$-derived materials. (a)-(d) TEM and high-resolution TEM images of VO-VC@800 sample revealing the crystalline nature of VO-VC particles (c) and amorphous nature of graphitic carbon in the prepared samples (d). (e) TGA-DTA curves of RB-$VOSO_4$. (f) XPS survey spectrum of VO-VC@800, (g) high-resolution XPS spectra of V 2p and O, and (h) high-resolution C 1s spectrum shows dominant sp^2/sp^3 carbon, along with C-O and C=O functionalities, confirming the formation of conductive carbon matrices obtained from the bread-derived food waste.

View Article Online
DOI: 10.1039/D6TA01506A

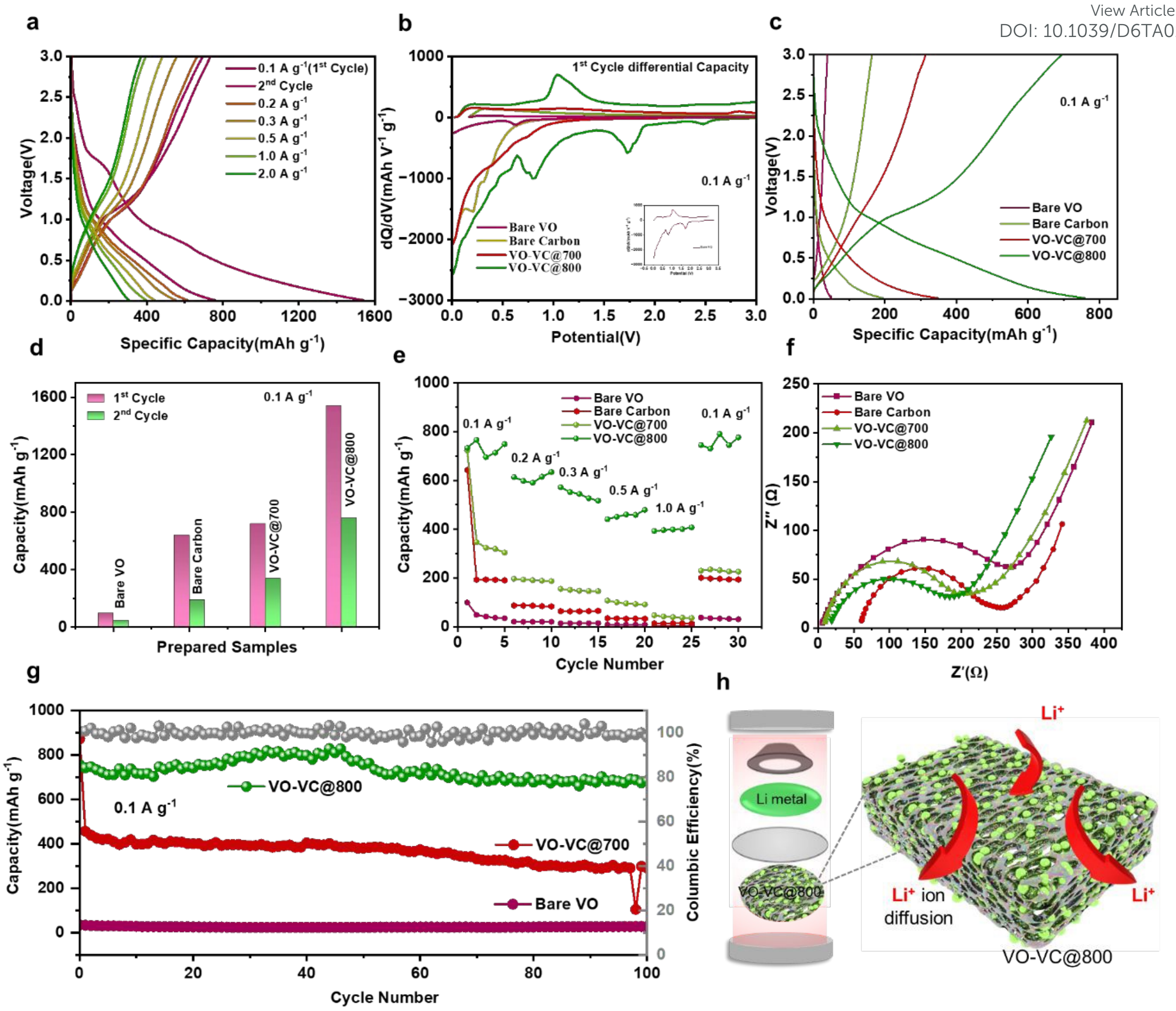

Figure 5. Electrochemical performance of bare VO, bare carbon (without vanadium) and VO-VC@carbon-based anodes for Li-ion batteries. (a) Galvanostatic charge-discharge profiles of the VO-VC@800 electrode measured at various current densities (0.1-2 A g^{-1}), (b) Differential capacity (dQ/dV) curves and (c) comparative charge-discharge capacities of bare VO, bare carbon, VO-VC@700, and VO-VC@800 electrodes measured at 0.1 A g^{-1} during the 2nd cycle. (d) Comparative capacity loss of the four electrodes from the 1st to 2nd cycles. (e) Rate capability of the electrodes was evaluated at different current densities, confirming the superior rate performance of VO-VC@800. (f) Nyquist plots of bare VO, bare carbon, VO-VC@700, and VO-VC@800-based Li-based cells, showing reduced charge-transfer resistance for the VO-VC@800 cell. (g) Long-term cycling stability of the VO-VC@800 electrode in

View Article Online
DOI: 10.1039/D6TA01506A

comparison with bare VO and VO-VC@700 and (h) Schematic illustration of the structural advantages of the VO-VC@800 composite during Li-ion energy storage.

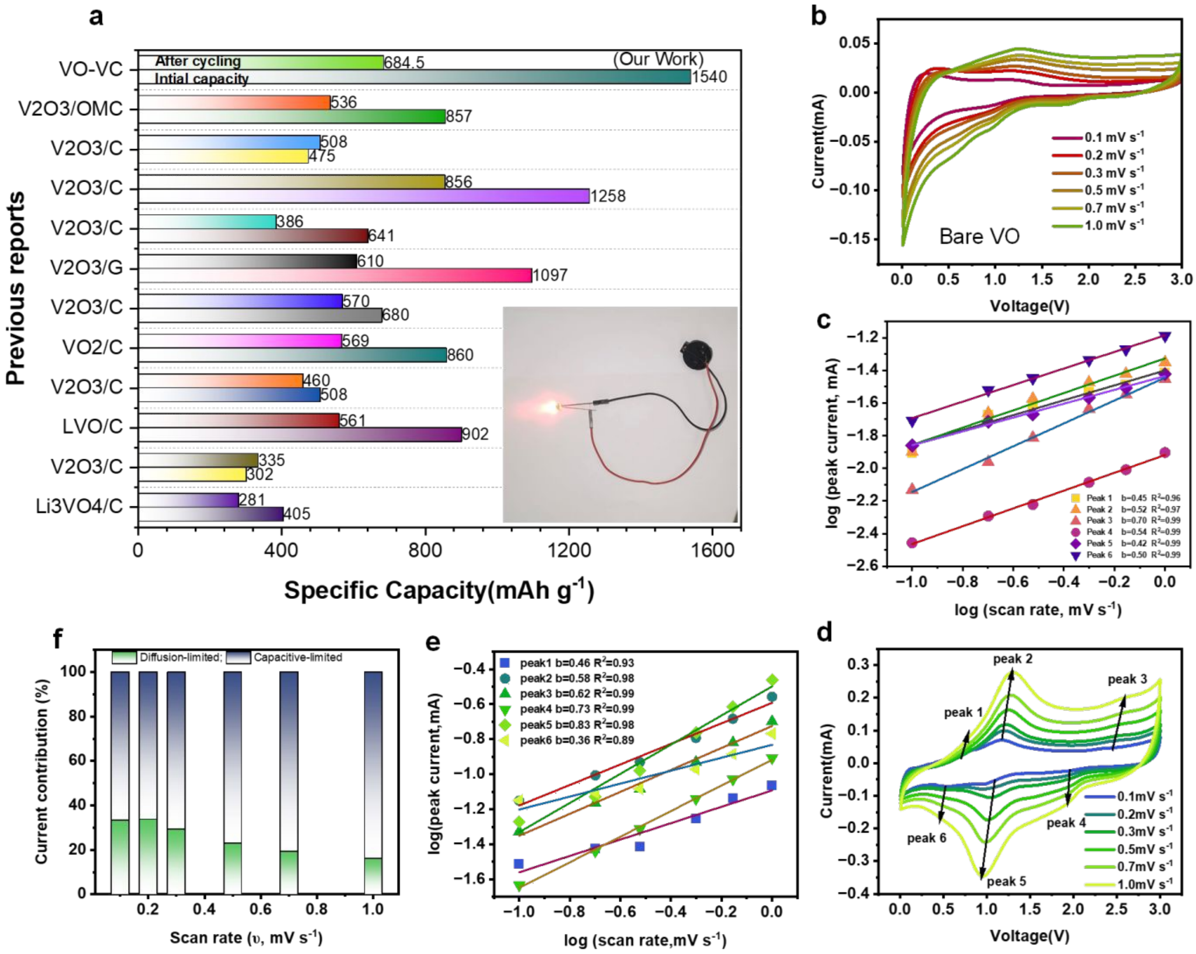

Figure 6. Comparative specific capacity (1st and last cycle capacity) of vanadium-based materials with our VO-VC@800 composite-based LiBs; inset shows a light-emitting diode powered by the assembled VO-VC@800//Li cell. (b) CV curves of the bare VO//Li cell recorded at different scan rates and (c) determination of the b-values from the linear fitting of peak current (i) and scan rate (v). (d) CV curves of the VO-VC@800//Li cell measured at various scan rates, showing well-defined redox peaks and improved electrochemical reversibility; (e) corresponding b-value analysis for VO-VC@800. (f) Quantitative separation of capacitive-controlled and diffusion-controlled contributions to the total charge storage.

View Article Online
DOI: 10.1039/D6TA01506A

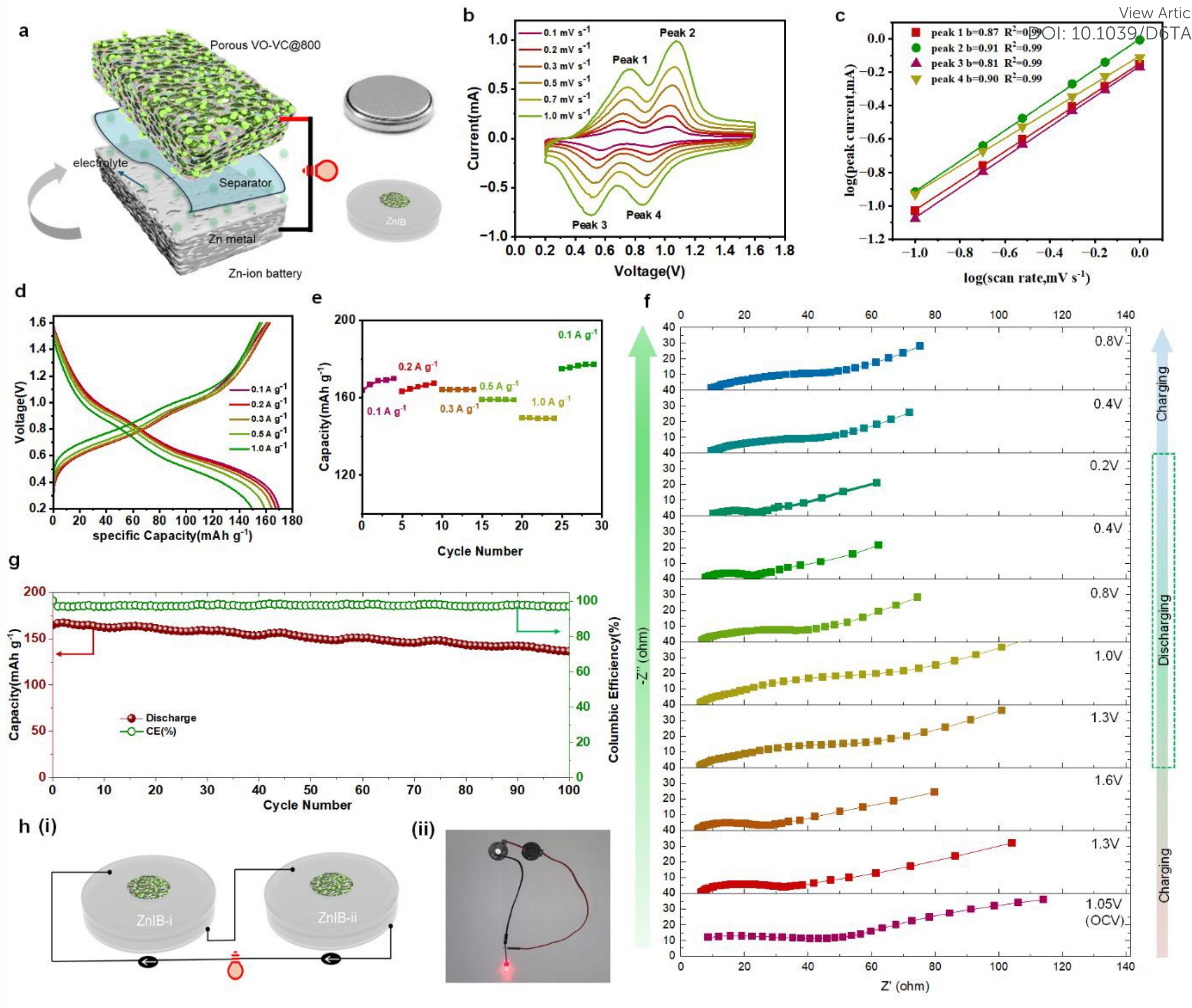

Figure 7. Electrochemical performance of VO-VC@800 material for aqueous ZiBs. (a) Schematic illustration of the assembled Zn//VO-VC@800 cell. (b) CV curves of the VO-VC@800 with different scan rates of 0.1-1.0 mV s^{-1}); c) determination of b-values derived from the relationship between peak current and scan rate. (d) Charge-discharge profiles measured at different current densities; (e) Rate capability of the VO-VC@800-based ZiB, highlighting excellent rate performance and recovery. (f) *In-situ* EIS plots of the ZIB collected during charge and discharge process at different cell voltages; (g) long-term cycling stability of the Zn–VO-VC@800 cell. (h) schematic of a series connected two ZiB and a photograph of two serially connected Zn//VO-VC@800-coin cells glowing a red color LED.

View Article Online
DOI: 10.1039/D6TA01506A

- The data supporting this article have been included as part of the Supplementary Information. Supplementary information: Table S1; Figure S1, S2 and Figure S3 and further experimental details. See DOI: [https://doi.org/DOI]